ELSEVIER

Optics and Lasers in Engineering 40 (2003) 263–288

OPTICS and LASERS in ENGINEERING

An experimental study of impact-induced failure events in homogeneous layered materials using dynamic photoelasticity and high-speed photography

L. Roy Xu[a,*], Ares J. Rosakis[b]

[a] *Department of Civil and Environmental Engineering, Station B351831, Vanderbilt University, Nashville, TN 37235, USA*

[b] *Graduate Institute of Technology, California Aeronautical Laboratories, Pasadena, CA 91125, USA*

Abstract

The generation and the subsequent evolution of dynamic failure events in homogeneous layered materials that occur within microseconds after impact were investigated experimentally. Tested configurations include three-layer and two-layer, bonded Homalite specimens featuring different bonding strengths. High-speed photography and dynamic photoelasticity were utilized to study the nature, sequence and interaction of failure modes. A series of complex failure modes was observed. In most cases, and at the early stages of the impact event, intra-layer failure (or bulk matrix failure) appeared in the form of cracks radiating from the impact point. These cracks were opening-dominated and their speeds were less than the crack branching speed of the Homalite. Subsequent crack branching in several forms was also observed. Mixed-mode inter-layer cracking (or interfacial debonding) was initiated when the intra-layer cracks approached the interface with a large incident angle. The dynamic interaction between inter-layer crack formation and intra-layer crack growth (or the so-called "Cook–Gordon Mechanism") was visualized for the first time. Interfacial bonding played a significant role in impact damage spreading. Cracks arrested at weak bonds and the stress wave intensity was reduced dramatically by the use of a thin but ductile adhesive layer.

Keywords: Impact failure; Layered materials; Interfacial bonding; Dynamic photoelasticity; High-speed photography

*Corresponding author. Fax: +1-615-322-3365.
E-mail address: l.roy.xu@Vanderbilt.edu (L.R. Xu).

0143-8166/03/$ - see front matter
PII: S0143-8166(02)00093-3

1. Introduction

Layered materials and structures have promising applications in many important fields of engineering. These include, among others, the use of advanced composite laminates in aerospace engineering; sandwich structures in naval engineering; and multi-layered thin film structures in micro-electronic-mechanical systems. In an entirely different length scale such materials are also found in the complex layered rock structures of earth's crust. While failure characteristics of layered materials subjected to static loading have been investigated extensively in past years [1], their dynamic counterparts have remained elusive. Our current research interest focuses on studies of such dynamic failure events in layered materials and, in particular, on the identification of the chronology and sequence of these events. For most layered materials, the presence of highly complicated dynamic failure modes and the inaccessibility of internal damage to real-time scrutiny has resulted in experimental studies of only the final impact damage characteristics and to the measurement of post-mortem residual strengths [2–4]. Hence, the sequence and nature of failure process have never been properly clarified.

For many simple engineering structures subjected to static or dynamic loading, computational and analytical models can be employed to provide realistic approximations of the physical failure processes under investigation. However, this may not be possible when more complex geometries, involving layered materials or configurations, need to be investigated. For such more complex cases, model experiments may prove extremely useful as intermediate steps, which reveal the basic physics of the problem and provide relatively straightforward validation of computational models before such models are applied to predictions of the fully complex failure situations. A striking example of the role of model experiments was provided by Riley and Dally [5], who designed a model metal/polymer layered specimen subjected to dynamic loading. Their model configuration was designed to simulate dynamic loading and stress wave evolution in complex layered structures.

In our experiments, we adopt and extend the same concept and to that effect we introduce an appropriate intermediate model configuration, which allows us, in addition to stress wave loading, to study the basic dynamic failure mechanisms involved in a layered structure. Indeed, in order to simulate the difficult 3-D problem of the out-of-plane impact of real layered structures and at the same time preserve the essence of the failure phenomena involved, we propose a two-dimensional, plane stress specimen, which represents a cross-sectional cut from a layered structure as illustrated in Fig. 1. For this type of model specimens, failure processes are easy to record, visualize and analyze. It is noted that although the exact impact mechanics involved in these two configurations are not identical (mainly because of dimenionality constraints), the general mechanisms of stress wave propagation and failure progress of the real and model layered materials are quite similar.

As discussed by Xu and Rosakis [6], in designing these model two-dimensional specimens, it is important to select model materials whose elastic mismatch is similar to that of materials used in real engineering applications. Selecting similar Dundurs' parameters [1] may ensure similarity of the elasto-static response. Meanwhile,

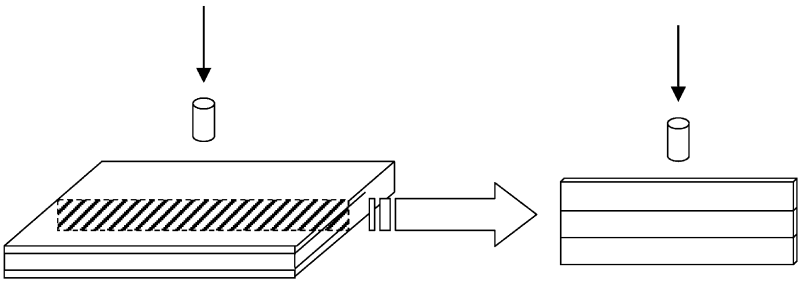

Fig. 1. 3-D problem and plane stress idealization.

selecting model material combinations with similar ratios of wave speeds as the real structure is important in considering similarity of their elasto-dynamic behaviors. These two issues form similarity rules to connect real structures and experimental models. In the present investigation, we only study layered materials composed of one kind of homogeneous material. For this zero stiffness-mismatch case, both Dundurs' parameters vanish and the ratio of wave speeds is unity. The resulting layered structure is constitutively homogeneous and it only features planes of strength and fracture toughness inhomogeneity (bonds lines) between layers. In the absence of constitutive material property mismatch, our major purpose is only to explore the effect of interfacial bonding on the development of dynamic failure mechanism in layered materials.

The objectives of the current work are to conduct systematic experimental studies of the time evolution and the nature of different failure events and to investigate the interaction of these dynamic failure modes in real-time. Through these model experiments, we try to provide guidance for the construction of theoretical models and validation of numerical codes.

2. Experimental program

2.1. Materials and specimens

Homalite-100 was selected as our model photoelasticity material. Some of its physical properties are listed in Table 1. The quasi-static values are obtained from the literature while the dynamic values are measured by the procedure outlined in Section 3. The dynamic fracture characteristics of bulk Homalite-100 have been well investigated in the past decades [7–10]. Here, we mainly pay attention to the dynamic failure modes of Homalite in layered form. To provide different interfacial strengths and fracture toughnesses, four kinds of adhesives, Weldon-10 and Loctite 330, 384 and 5083, were used to bond the interfaces [11]. The interfacial bond strengths and the fracture toughness for those adhesives are listed in Table 2. The Weldon-10 and Loctite 330 are considered to be "strong" adhesives. The Loctite 384 can form an

Table 1
Material properties of Homalite–100

Property	Homalite 100	
	Static (strain rate $\sim 10^{-3}$/s)	Dynamic (strain rate $\sim 10^{3}$/s)
Density ρ (kg/m^3)	1230	1230
Young's modulus (GPa)	3.45	
Dilatational wave speed c_l (m/s) (plane stress)	1890	2119
Shear wave speed c_s (m/s)	1080	1208
Rayleigh wave speed c_R (m/s)	1010	1110
Poisson's ratio v	0.35	0.35
Material fringe constant f_σ (kN/m)	23.7	

Table 2
Interfacial strengths and model I fracture toughness of different bonds

Interface	Tensile strength σ_c (MPa)	Shear strength τ_c (Mpa)	Fracture toughness (MPa m$^{1/2}$)	G_{IC} (J/m^2)
Homalite//Weldon-10//Homalite	7.74	>21.65	0.83	199.7
Homalite//330//Homalite	6.99	12.58	0.93	250.7
Homalite//384//Homalite	6.75	7.47	0.38	41.9
Homalite//5083//Homalite	1.53	0.81	0.19	10.5

"intermediate strength" bond while the Loctite 5083 gives a "weak bond". The thickness of the final adhesive layer is $<20\,\mu$m. Loctite 5083 adhesive is also considered to be a ductile adhesive since its elongation at failure (as measured by the manufacturer) in cured bulk form is 170% or two orders of magnitude higher than the rest of the adhesives.

Three different types of specimens were designed and tested. As shown in Fig. 2, type-A specimens have two layers with equal layer widths, and type-B specimens involve two layers with one layer twice as thick as the other. Type-C specimens were designed to have two bonding interfaces and three equal-width layers. All three types of specimens have the same out-of-plane thickness of 6.35 mm (0.25 inch) and the same length of 254 mm (10 inches). In general, each layer width is 33 mm except for a few specimens in which $w_1 = 38.1$ mm.

2.2. Experimental setup

A schematic of the dynamic photoelasticity setup used in this study is given in Fig. 3. Two sheets of circular polarizer were placed on either side of the specimen. An Innova Sabre argon-ion pulsed laser was used as the light source. The laser was set to operate on a single wavelength—514.5 nm (blue–green light). At this wavelength, the continuous power output of the laser is 8 W. The laser emits an

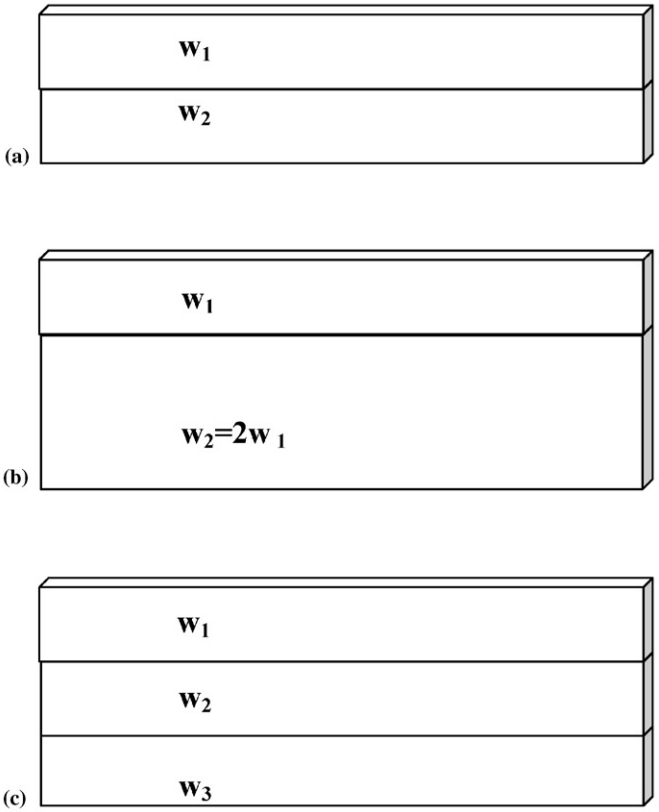

Fig. 2. Model specimen geometries: (a) two-layer specimens with equal widths (type-A), (b) two-layer specimens with $W_2 = 2W_1$ (type-B), and (c) three-layer specimens with equal widths (type-C).

intense beam of 2 mm diameter, which is 100:1 vertically polarized. An acousto-optic modulator (Bragg cell) is placed in front of the laser to produce a pulsed output. The duration of each laser pulse can be varied between 8 and 20 ns. During the impact experiment, the acousto-optic modulator is driven by the high-speed camera to control the timing of each laser pulse, so that it coincides with the times the camera optics are aligned to expose a particular frame on the film track. An electro-mechanical shutter is placed in front of the laser to prevent the light "leaking" through the Bragg cell from exposing the film before or after the experiment. A wide gap sensor mounted on the gas gun barrel about 1 in from the end is used to trigger the shutter opening for a short duration (around 10 ms). A strain gage bonded to the specimen at the impact side was used to trigger recording by the high-speed camera. The coherent, monochromatic, plane polarized light output is collimated to a beam of 100 mm diameter. The laser beam is transmitted through the specimen. The resulting fringe pattern is recorded by the high-speed camera.

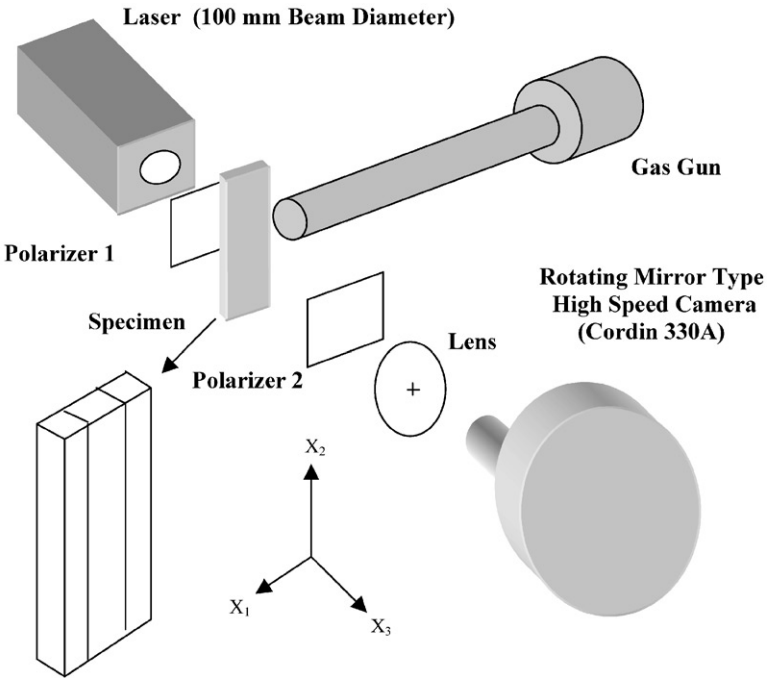

Fig. 3. Schematic of the dynamic photoelasticity setup.

A Cordin model 330A rotating mirror type high-speed film camera was used to record the images. The high-speed camera contains a rotating mirror that directs the image on to the film mounted on a film track surrounding it. The rotating mirror is driven by a gas turbine running on compressed helium. Individual frames are exposed sequentially by inducing the laser to produce a high-powered pulse of short duration and when the rotating mirror is aligned to a particular frame. The camera records 80 distinct images at frame rates of up to 2 million per second. A feedback signal from the turbine is fed to a 10 KHz frequency counter, which allows a precise monitoring of the turbine speed. Also, the synchronizing signal sent by the camera to the acousto-optic modulator is simultaneously routed to a HP digital oscilloscope to obtain a record of the timings of each individual laser pulse. Kodak TMAX 400 black and white film was used to record the fringe patterns. The optical system in the high-speed camera introduces an elliptical distortion to the recorded films. For a circular original image, the recorded image is an ellipse with its major axis about 15% larger in comparison with the minor axis. The developed negatives were scanned using a negative scanner and the elliptical distortion was removed digitally.

During the impact test, a projectile was fired by the gas gun and hit the specimen or a steel buffer to trigger the recording system. Under the dynamic deformation, the generation of isochromatic fringe patterns is governed by the stress optic law. For the case of monochromatic light, the condition for the formation of isochromatic

interference fringes can be expressed as [7]

$$\hat{\sigma}_1 - \hat{\sigma}_2 = \frac{Nf_\sigma}{h},$$

where $\hat{\sigma}_1 - \hat{\sigma}_2$ is the principal stress difference of the thickness averaged stress tensor, f_σ is the material fringe value which is listed in Table 1, N is the isochromatic fringe order and h is the half specimen thickness. The isochromatic fringe patterns observed are proportional to contours of constant maximum shear stress, $\hat{\tau}_{\max} = (\hat{\sigma}_1 - \hat{\sigma}_2)/2$.

2.3. The three-lens system

In order to observe remote failure event interactions, a large field of view is necessary. However, our Cordin 330A camera has a long front optical tube and its maximum view angle 2β is 4° as shown in Fig. 4. If a single lens is used, the maximum size of the field of view is 2f tan (β), were f is the focal length of the lens. In order to minimize shadow spot formation, f should be chosen to be a small value based on our practical experience. As a result, the resulting field of view will be too small for full specimen visualization. To overcome this problem, a three-lens system is employed as shown in Fig. 4. In this system, the first lens facing the 100 mm laser beam is a plano-convex lens whose focal length is 380 mm. The second lens is a plano-concave lens whose focal length is 100 mm. Lenses 1 and 2 share the same focal point at one side and, as a result, a parallel beam of reduced diameter is formed. This beam passes through a bi-convex lens (lens 3) of focal length 500 mm. The resulting converging beam incident angle is $<2^\circ$ and satisfies our stated requirement. Hence, the full 100 mm beam can enter the long camera tube.

Another restriction governing the choice of lens types and focal lengths comes from aberration balancing. Here, the convex side of lens 1 and the planar side of lens 2 must face the laser beam to cancel part of the aberration. The most significant shortcoming for this three-lens system is its alignment sensitivity. In addition, light intensity is somewhat reduced after the beam passes from this multiple lenses arrangement. So, this system was used only for those experiments, which required a large field of view.

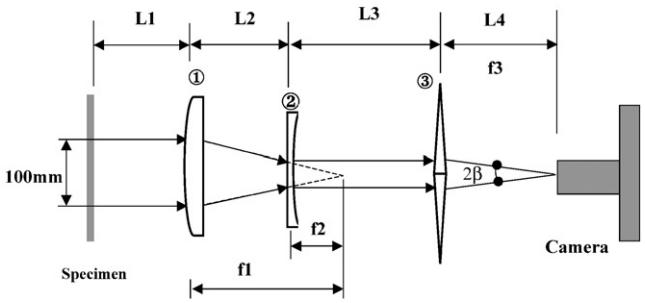

Fig. 4. The three-lens system used in large field of view experiments. (1) plano-convex lens, (2) plano-concave lens, and (3) bi-convex lens.

3. Results and discussion

Homalite-100 is a rate sensitive viscoelastic solid and its wave speeds depend on strain rate as indicated in Table 1. Wave speed differences of approximately 17% are expected over six orders of magnitude differences in equivalent strain rate. In order to obtain a more accurate measure of the wave speed levels relevant to our impact experiments, a calibration test was undertaken. A Homalite plate was impacted at a projectile speed of 24 m/s and the impact area was imaged by the high-speed camera. The photoelastic fringe pattern corresponding to this dilatational front spread through the material and the location of its front was traced and plotted as a function of time (see Fig. 5). The resulting linear variation reveals a constant dilatational wave speed of approximately 2119 m/s which, for a Poisson's ratio of 0.35, corresponds to a shear wave speed of 1208 m/s and a Rayleigh speed of 1110 m/s. Fringe patterns of the type shown in Fig. 5 have also allowed us to estimate the local strain rate at the impact point. For the impact speeds used in this paper, the strain rate was found to be of the order of 10^3/s. As expected these values are higher than the ones corresponding to a quasi-static loading (strain rate $\sim 10^{-3}$/s) and are listed in a separate column of Table 1. From now on indicated wave speeds will correspond to the above measured dynamic values.

3.1. The two-layer specimen with equal layer widths subjected to mitigated projectile impact

Fig. 6 shows a series of photoelasticity snap shots following impact of a type-A specimen. In all experiments reported in this section, the projectile impacted the center of the bottom layer on a steel buffer as shown in Fig. 6(a). The horizontal line in the field of view reveals the position of the interface in which the dark circular spot, at the lower left-hand side just below the interface, is a scaling mark of 6.35 mm

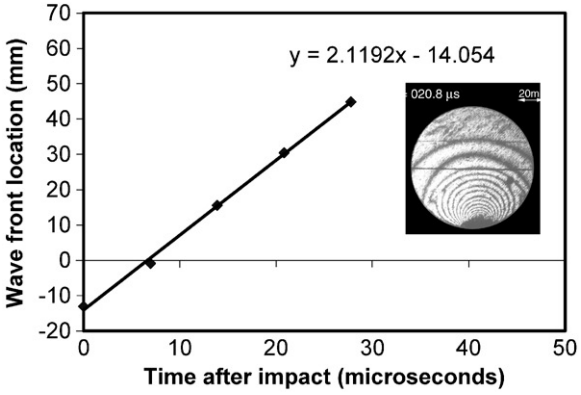

Fig. 5. Measured stress wave front location versus time used to estimate the longitudinal wave speed of the Homalite-100 subjected to the current impact strain rate regime.

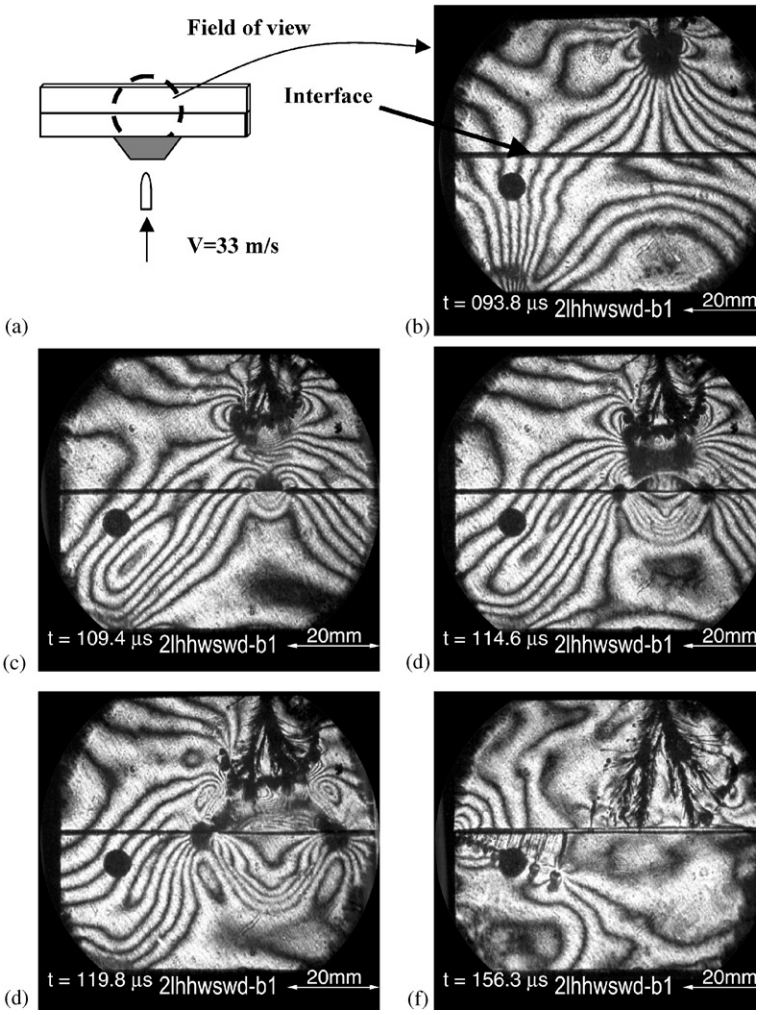

Fig. 6. Dynamic failure process in a two-layer specimen showing the interaction of a fan of mode I incident cracks and the resulting interfacial crack. The thin horizontal line is the weak interface. The circular dot at the left low position in every photo is the scaling mark bonded on the specimen.

in diameter. Fig. 6(b) shows a fan of mode I cracks (symmetric fringe patterns) appearing from the upper free edge at approximately 93.8 μs after impact. Generally, the whole recording system has a delay and its timing error is within 10 μs. After impact, the longitudinal compressive stress wave traveled from the lower impact side towards the upper free edge. This compressive stress wave reflected from this edge as a tensile wave and its intensity was sufficient to nucleate a fan of branched cracks from the free edge. As time goes on (Fig. 6(c)–(f)), the nucleated fan of cracks widens significantly by producing a multiplicity of both successful and unsuccessful branches (for a discussion of crack branching phenomenon in bulk Homalite, see

Ravi-Chandar and Knauss [10]), some of which move towards the still coherent interface. The average speed of these locally mode I, branched cracks is 0.41 C_S, which is the branching speed in bulk Homalite.

Well before the branched cracks reached the interface, a central inter-layer crack was nucleated at the intersection of the specimen centerline and the bond line as seen in Fig. 6(c). This interfacial crack propagated in both directions off the center as shown in Fig. 6(d). At the specimen centerline, the shear stresses vanish because of symmetry. As a result, the nucleated inter-layer crack is initially and, for a very short time, mode I dominated. Its nucleation is induced by the stress field produced by the fan of branched cracks approaching the interface. As this crack spreads symmetrically, opening up the interface (see distinct evidence of decohesion in Fig. 6(f)), the fan of branched cracks discelerates and arrests just before these cracks reach the decohered interface. The above described scenario is perhaps the first real-time visualization of the dynamic equivalent of the "Cook–Gordon Mechanism" [12] describing the remote decohesion of an interface due to the approach of a matrix (intra-layer) crack.

As the interfacial crack spreads away from the specimen centerline, it almost immediately encounters increasing amount of interfacial shear stress, which quickly converts it to a mixed-mode and eventually to a mode II dominated crack. Unlike propagating cracks in bulk Homalite, interfacial cracks are constrained to propagate along the weak interface and, as a result, they can do so under mixed-mode or primarily mode II conditions. They can also propagate at very high (even inter-sonic) speeds compared to their bulk (intra-layer) counterparts. This phenomenon has recently been investigated experimentally by Rosakis et al. [13] and numerically by Needleman [14] and by Geubelle and Kubair [15]. To illustrate this point, the variation of the left interfacial crack tip position versus time and the corresponding crack tip speed are plotted in Fig. 7(a) and (b), respectively. Indeed this figure shows very high interfacial crack tip speeds initially well within the intersonic regime (crack speed is greater than the shear wave speed but less than the longitudinal wave speed of the bulk material), later decelerating to a large fraction of the Rayleigh wave speed. This observation is consistent with the surmised shear-dominated nature of this crack (see Geubelle and Kubair [15]). If this inter-layer crack is, at least for short times, intersonic, the photoelastic images obtained here should reveal the existence of shear shock wave discontinuities emitted from the propagating crack tips and inclined at an angle $\beta = \sin^{-1}(C_s/V)$ to the interface (Rosakis et al. [13]). Indeed, a close look at Fig. 6(d) and (e) reveal the existence of such shear shock waves, which are shown in detail in Figs. 8(a) and (b). The angle β can now be used to provide an independent measure of the ratio, V/C_s of the instantaneous crack tip speed to the shear wave speed. This ratio is plotted in Fig. 8(c) as a function of time (black triangles). For comparison purposes, the same ratio, obtained from the independent measurement of the crack length record is also shown. The two sets of points are obtained by using crack speeds from Fig. 7 and the quasi-static and the dynamic values of C_s, from Table 1, respectively. As evident from this composite plot, the trends are very consistent. Differences are due to experimental errors introduced through differentiating the crack length record, and uncertainties in shear wave

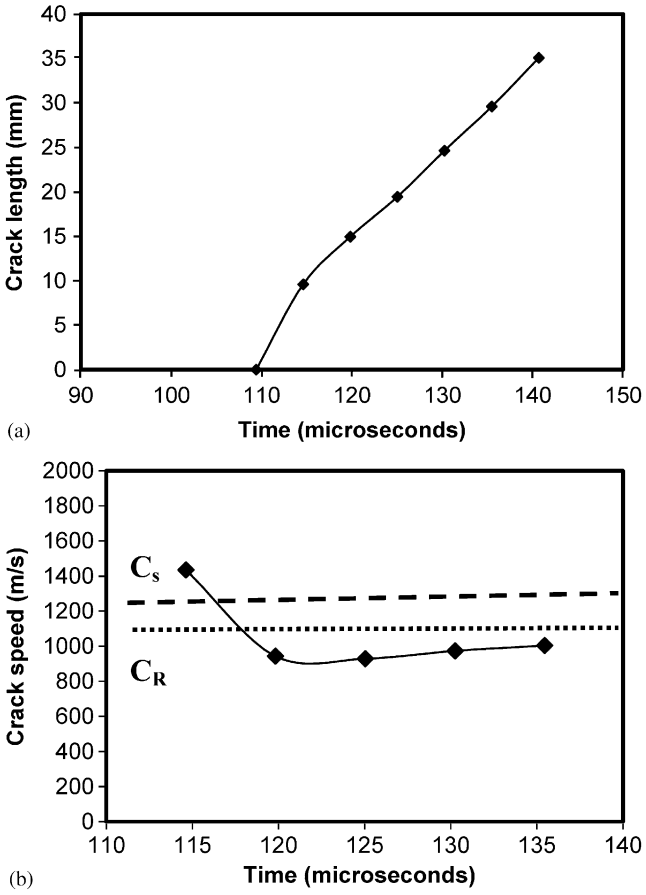

Fig. 7. History of inter-layer crack length (a) and speed (b) of the two-layer specimen (2lhhwswd-b1). The two horizontal lines correspond to the dynamic values of the shear and Rayleigh wave speeds of Homaite-100 shown in Table 1.

speed choice. Indeed very near the crack tip where the strain rates are very high, the dynamic values of shear wave speed should be used; while further away the static values may be more appropriate for shock angle estimation (Abraham and Gao [16]).

Additional evidence of the shear-dominated nature of the interfacial cracks is provided by the nucleation and growth of a periodic array of secondary microcracks observed to occur along the bond at a certain distance from the centerline of the specimen (see Fig. 6(f)). These microcracks are generated just behind the propagating shear crack tip (see Fig. 9) and spread at a steep angle of approximately 11° to the normal of the bonded interface. They are locally mode I cracks and they grow only at the bottom layer side of the interface indicating that this layer is primarily in tension along the horizontal direction. Their opening nature is evident

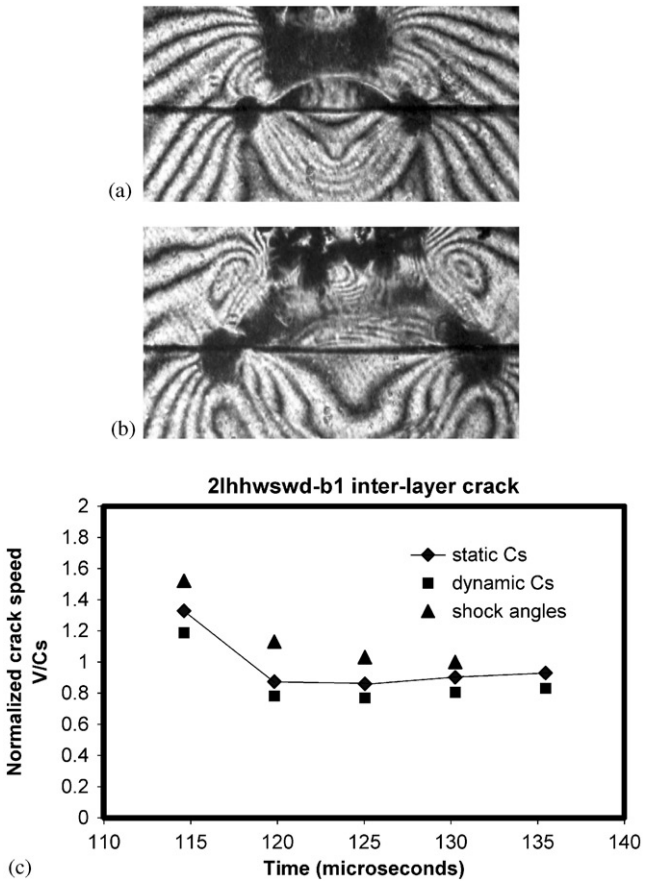

Fig. 8. Early stages of intersonic, interfacial crack growth revealing the existence of shear shock waves (a, b) and the estimated interfacial crack speeds using different methods (c).

from the existence of symmetric and almost circular caustics surrounding their tips (see Fig. 9). The generation of such secondary cracks following shear interfacial crack growth was first discussed by Rosakis et al. [17] and Samudrala et al. [18] in connection to intersonic shear rupture of Homalite/Homalite interfaces. As discussed in these references, their 11° inclination indicates the existence of frictional contact and sliding behind the growing shear crack faces, which slightly change the principal stress directions responsible for path selection for the microcracks.

For the present discussion, the existence of such secondary cracks in impacted layered specimens is also very important. It shows how different failure modes (some symmetric and others shear-dominated) may interact and trigger each other in a non-straightforward way to result in the final brittle failure of a layered structure. Indeed in the processes discussed above, damage was first initiated by the mode I dominated fan of branched cracks moving towards the interface. Without penetrating the

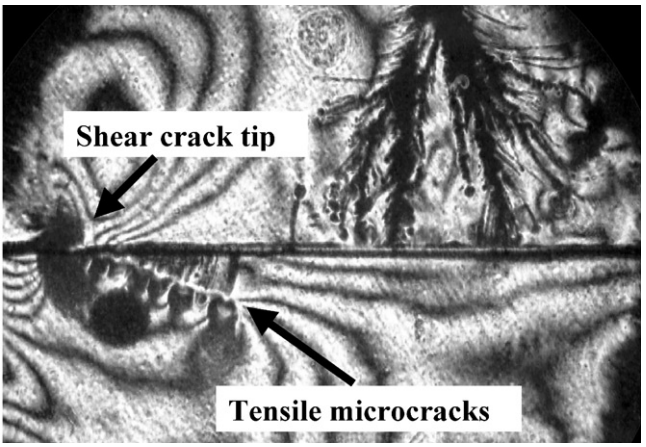

Fig. 9. A detailed view of the formation of secondary opening microcracks following shear dominated interfacial delamination.

interface, this fan of opening crack induced inter-layer failure which in turn transitioned from an opening mode to a shear mode as it moved away from the centerline and as it delaminated the interface. Finally, it was this shear-dominated delamination stage which made it possible for the periodic sequence of opening microcracks to penetrate the bottom layer and cause its final fragmentations.

3.2. The two-layer specimen with equal layer widths subjected to direct projectile impact

Fig. 10 shows a series of images for a two-layer specimen subjected to direct projectile impact. Stress wave propagation and reflection from the top free edge is shown in Fig. 10(b). The fringe pattern at the bonded interface is continuous and does not even exhibit any discontinuities in slope. This implies a good bonding and matched material properties of the Homalite and the bonding adhesive. Unlike the previous specimen with a mitigating steel buffer at the impact point, a dark zone of diffuse damage was observed at the impacted side. This dark zone is a highly compressed zone of comminuted material created by the direct projectile impact. Due to the large out-of-plane deformation, the light rays transmitted through this area cannot be collected by the high-speed camera, thus producing a massive shadow spot. It is also noticed that a "plastic deformation ring," initially propagating at approximately 118 m/s, appeared at approximately 76 μs (Fig. 10(c)). Across this ring, permanent discontinuities of the fringe pattern were observed, indicating the irreversible damage nature within this semi-circular region. At the first stages of its evolution, the plastic semi-circle was smooth and transparent. As time evolved several radial mode I cracks radiating from the impact point crossed the ring boundary moving towards the upper free edge of the specimen. With increasing time, the initial transparency of the plastically deformed area surrounded by the ring was

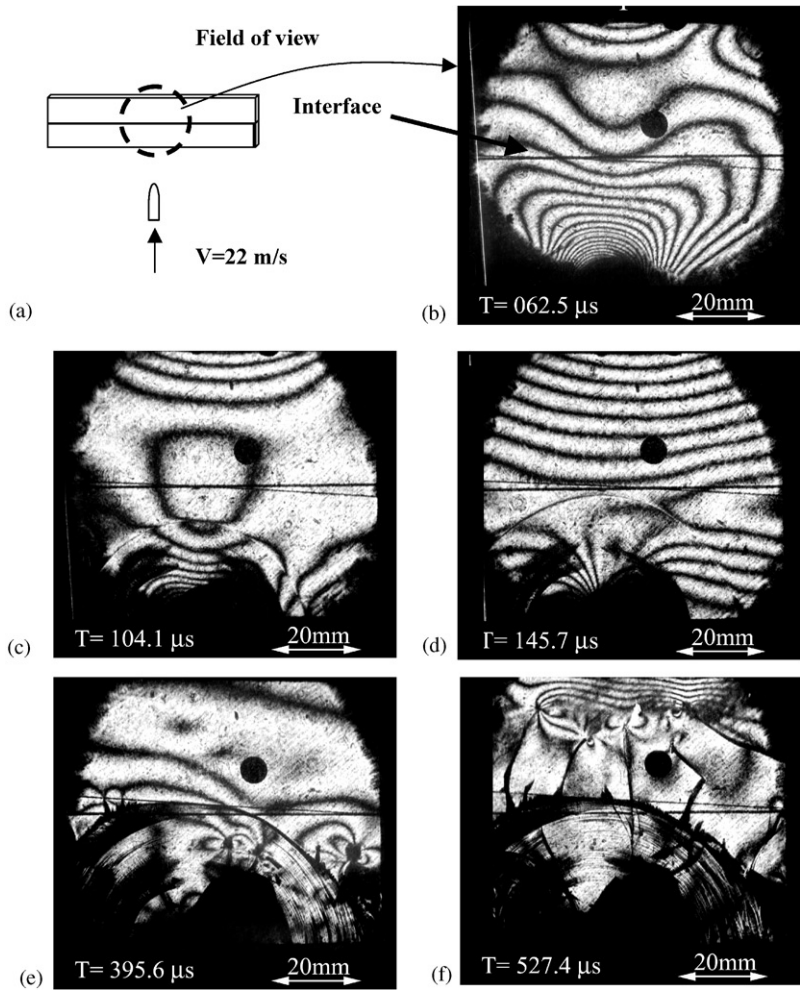

Fig. 10. Failure process of a two-layer specimen (2lhhsp384-1) subjected to direct projectile impact.

compromised by the spreading of more complex 3-D damage modes. This became obvious through post-mortem inspection of the impacted plates where large 3-D surface cracks propagating in the specimen thickness (parallel to the plate free surface) were identified. It is the evolution of such cracks and their slightly wavy nature that produce the ''shell'' like structure of the further damaged plastic semi-circle in Fig. 10(e) and (f).

3.3. Failure process in a two-layer specimen with unequal layer widths

Post-mortem pictures of damage resulting from impact of two, type-B, specimens are shown in Figs. 11(a) and (b). The only difference between these two specimens,

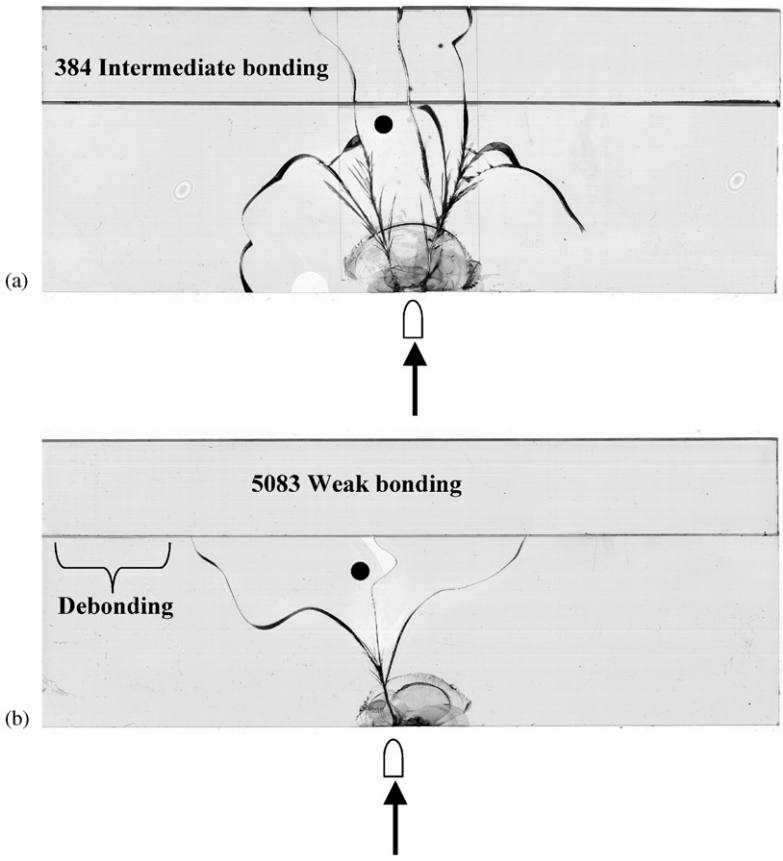

Fig. 11. Post-mortem failure patterns of two identical specimens with different interfacial bond strengths subjected to the same impact speed of $V = 20\,\mathrm{m/s}$. (a) 2LHHSP384-LT1 (two-layer system with 384 intermediate strength bonding and impact at the large width layer), (b) 2LHHSP5083-LT1 (with 5083 weak bonding).

subjected to identical impact histories, is the strength of interfacial bonding. It is obvious from this figure that the interfacial bonding plays a significant role in the overall dynamic failure process. For the specimen with the intermediate strength interface as shown in Fig. 11(a), there are many branched, locally mode I, cracks radiating from the site of impact. Some of these I cracks only passed through the interface and did not cause any debonding. In contrast, the specimen with the weak interface, shown in Fig. 11(b), features fewer cracks radiating from the site of impact. Two of these cracks arrested at the weak interface, while the third produced only partial interfacial debonding.

Fig. 12 shows a sequence of real-time images of the dynamic failure progress of the layered Homalite structure (type-B) featuring only one weak interface bond. This case corresponds to the post-mortem pattern of Fig. 11(b). In this sequence, the top horizontal line is the interface while the bottom line is a camera streak line of no

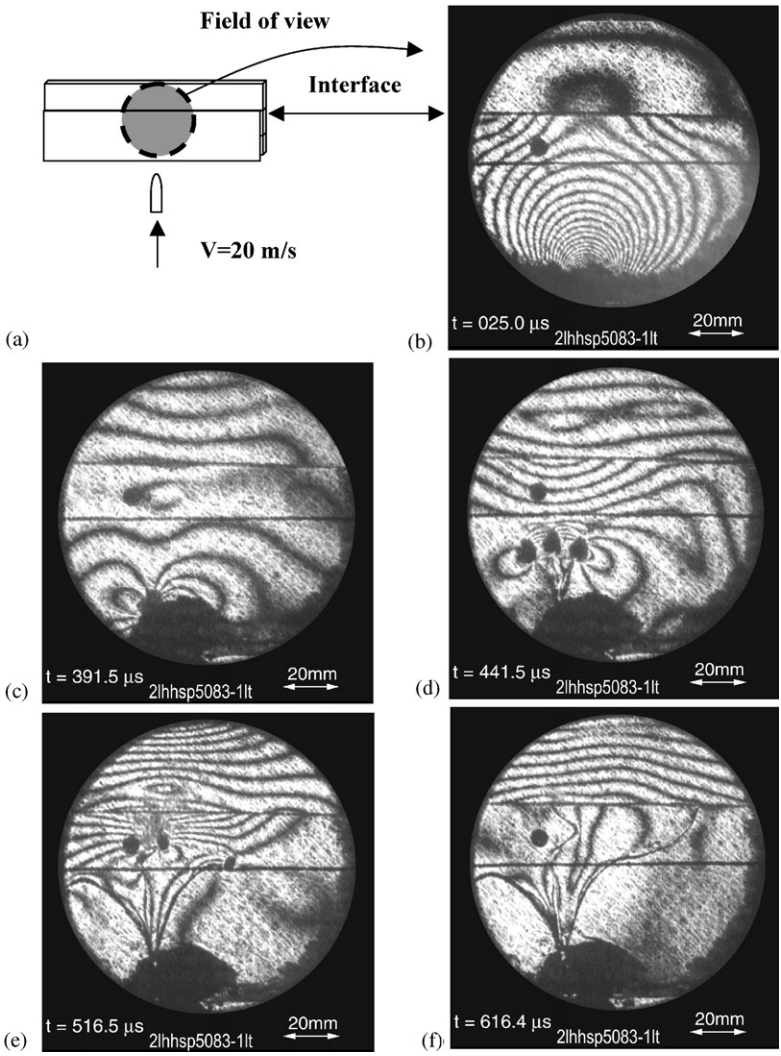

Fig. 12. Crack propagation and arrest at a two-layer specimen with 5083 weak bonding. The central black line is the camera streak reference line. The upper horizontal line is the only interface.

significance to the physical process. Fig. 12(b) reveals that the number of fringes or the stress wave gradient across the interface was dramatically reduced by the thin but soft adhesive film of 20 μm in thickness. After a long time period (380 μs) of wave motion within these two layers, a crack initiated from the dark impact zone was observed near the site of impact. This crack accelerated and eventually branched as shown in Fig. 12(d). As soon as the resulting branches approached the interface, they either arrested or turned into it producing partially interfacial debonding as shown in Figs. 12(e) and (f). The exact reasons of the inability of these cracks to penetrate the

upper layer are complex and are currently under investigation. However, the pivotal role of the weak interface in triggering this behavior is clearly evident. This may provide a useful design methodology to prevent the spread of impact damage resulting from low-speed projectiles. In an early study of impact mechanisms of composite laminates, Sun and Rechak [19] investigated a similar phenomenon by placing adhesive layers between plies, and thus delaying or even suppressing dynamic delamination.

In the case discussed above, the impact side was far away from the interface. If we now use the same specimen geometry and projectile loading history but instead impact the side close to the bonded interface, the resulting failure patterns are very different. This is evident from the post-mortem reconstructions of three bi-layer specimens (impacted close to the interface) with the same geometrical dimensions but different interfacial bonding strengths, which are presented in Fig. 13. It should first be emphasized that two identical specimens with the same interfacial bonding have quite different failure patterns if the impact location is reversed. This is evident by comparing Fig. 11(a) with Fig. 13(b) as well as Fig. 11(b) with Fig. 13(c). Differences are most pronounced for specimens with intermediate strength bonding shown in Figs. 11(a) and 13(b). Indeed more radial cracks were found and more extensive interfacial debonding occurred when the specimen was impacted closer to the bond. In the case shown in Fig. 13(b), it is also observed that cracks radiating from the impact point approached the bond with different incident angles (the angles between the crack path and the interface) and triggered a variety of subsequent failure behaviors. Those cracks with large incident angles penetrated the interface, but those cracks with small incident angles deflected into the interface and led to shear-dominated debonding, similar to the shear decohesion phenomenon discussed in Section 3.1. Here again, a close look at the upper side of the decohered interface reveals a periodic sequence of tensile microcracks inclined at small angles to the interface normal. These tensile microcracks are again generated as some of the radial cracks deflect into the interface, becoming shear-dominated and decohering it through a process of dynamic shear failure. The microcracks are generated just behind the growing shear interfacial cracks at the tension side of the interface. A real-time view of the failure process corresponding to an intermediate strength bond is provided in Fig. 14. The first failure event visualized in this sequence is the zone of comminuted and plastically deformed materials (dark area) as evident from Fig. 14(b). As time progresses, more than ten intra-layer radiating cracks appear and most of them pass through the interfacial bonding. The radial cracks that approached with a smaller incident angle, and were deflected into the interface, moved along it with higher speeds as evident by the elongated shape of the failure front arc shown in Fig. 14(c).

3.4. Failure process in a three-layer specimen with equal layer widths

Failure patterns became more complicated as a second interface was introduced to construct the three-layer specimens (type-C), shown in Fig. 15. Figs. 15(a) and (b) display post-mortem images of damage of two identical specimens featuring a strong

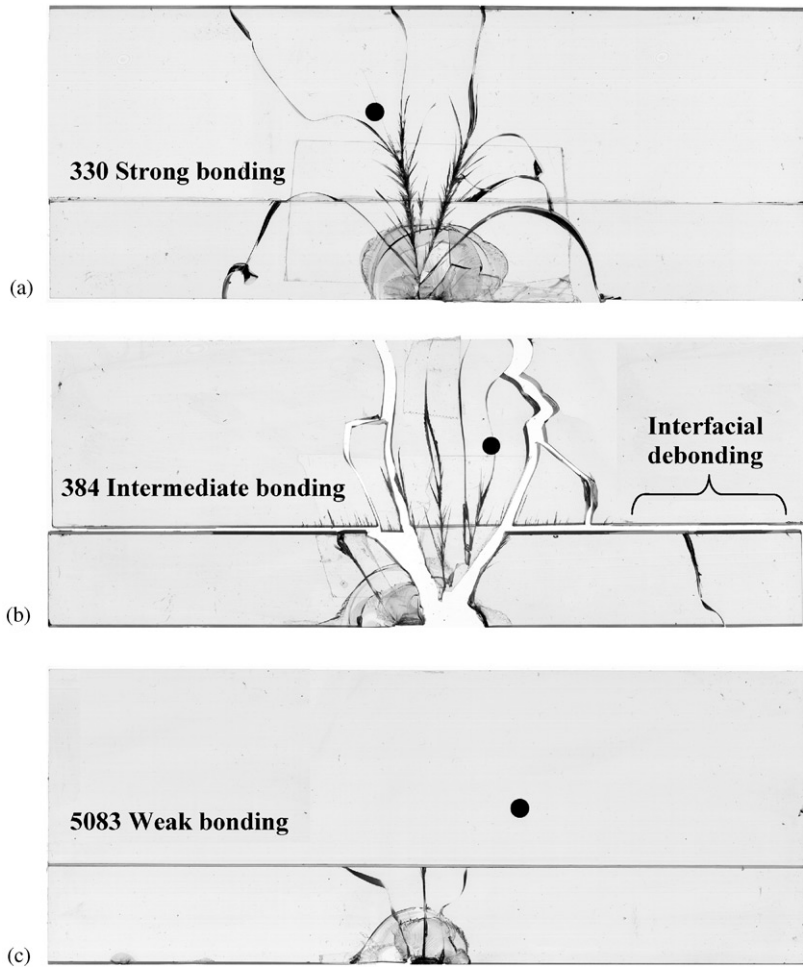

Fig. 13. Post-mortem failure patterns of three bi-layer specimens with different interfacial bonding strengths subjected to the same impact speed of $V = 21$ m/s. (a) 2LHHSP330ST1, (b) 2LHHSP384ST1, and (c) 2LHHSP5083ST2.

bottom interface and a top interface of two different (intermediate and weak) strengths, respectively. For the specimen with intermediate top interface (Fig. 15(a)), radial cracks initiated at the impacted layer and passed through the lower (strong) and the upper (intermediate) interfaces. Also, several cracks were able to cross all the way to the layer farthest from the impact side. In contrast, the specimen with the weak top interface, shown in Fig. 15(b), featured fewer radial cracks on the impacted side. Also, those cracks were arrested at the upper weak interface and did not penetrate into the upper layer. Extensive interfacial debonding at the upper interface was observed. The two specimens in Fig. 15(a) and (c) are identical except for the choice of impact side. In Fig. 15(a), the impact side is closer to the strong interface.

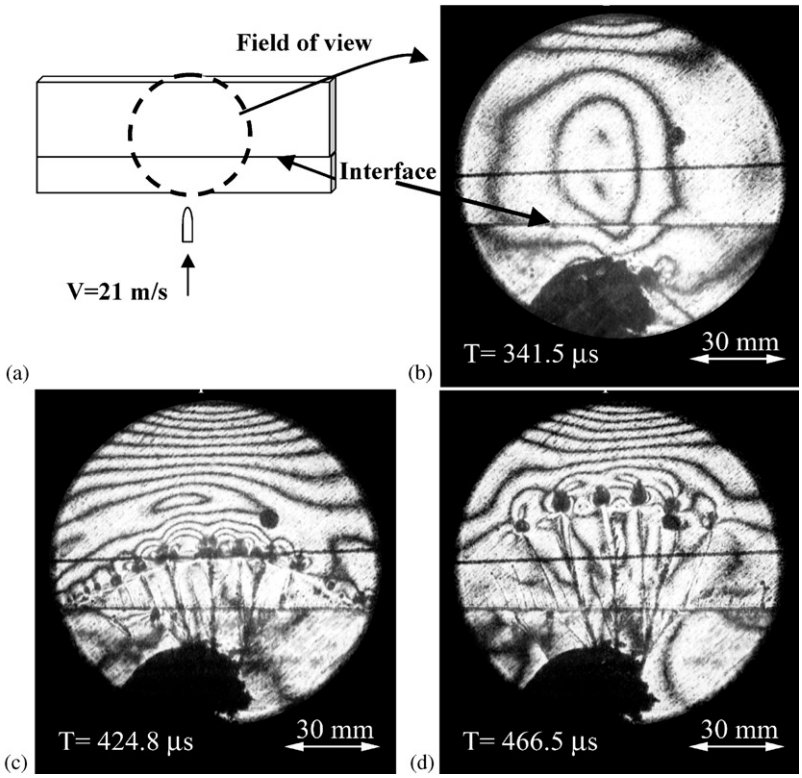

Fig. 14. A group of cracks initiated and propagated in a bi-layer Homalite specimen (2lhhsp384st1) with intermediate strength bonding. The lower thin line is the bonded interface. The upper horizontal line is a camera streak line.

So the radiating cracks mainly passed through this strong interface, causing debonding, only in the central portion of the specimen. Again debonding is shear-dominated because microcracks are visible along this decohered part of the strong bond.

A real-time view of the failure process of the specimen in Fig. 15(a) was presented in Fig. 16. In Fig. 16(b) the stress wave propagates through both upper and lower interfaces without experiencing any strong fringe or weak fringe slope discontinuities. In these photographs, the central thin line adjacent to the small circular mark is the camera streak line and is an artifact of the optical setup. The other two thin lines represent strong and intermediate strength interfaces. A group of radial cracks soon propagate through the lower, strong, interface as shown in Fig. 16(d) and (e). Those radiating cracks with large incident angles passed through the lower, strong interface and subsequently penetrated the upper, intermediate strength interface. Those few cracks that approached with smaller incident angles were deflected into the interface and one of them (moving to the right) is clearly shown in Fig. 16(d). To illustrate this phenomenon, an enlarged part of the specimen shown in Fig. 15(c) is

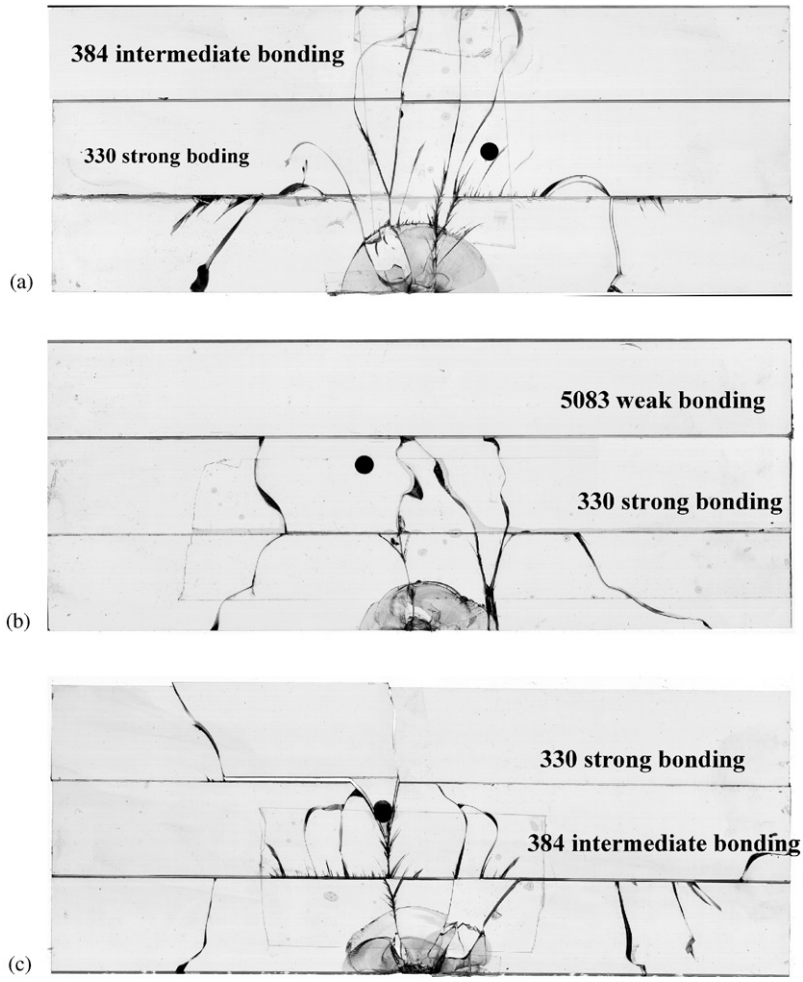

Fig. 15. Failure patterns of the three-layer specimens with different bonding and impact sides. (a) 3LHHSP330384-3302, (b) 3LHHSP330583-3301, and (c) 3LHHSP330384-3841. Notice specimens (a) and (c) are identical cases except for the different impact sides.

presented in Fig. 17. For two cracks with different incident angles, different failure events were observed. The crack with the large incident angle of 78° passed through the interface. However, the crack with the small incident angle of 50° could not penetrate the interface and created interfacial debonding. A systematic study of this problem is presently underway by the authors [20].

We now turn attention to tri-layer specimens involving at least one weak bond (the 5083 adhesive in Table 2). As clearly shown in Fig. 18, this adhesive is weak and ductile enough (see Section 2.1) never to allow crack penetration into the next layer under low-speed impact. In Fig. 18(a) some radial cracks from the impact region

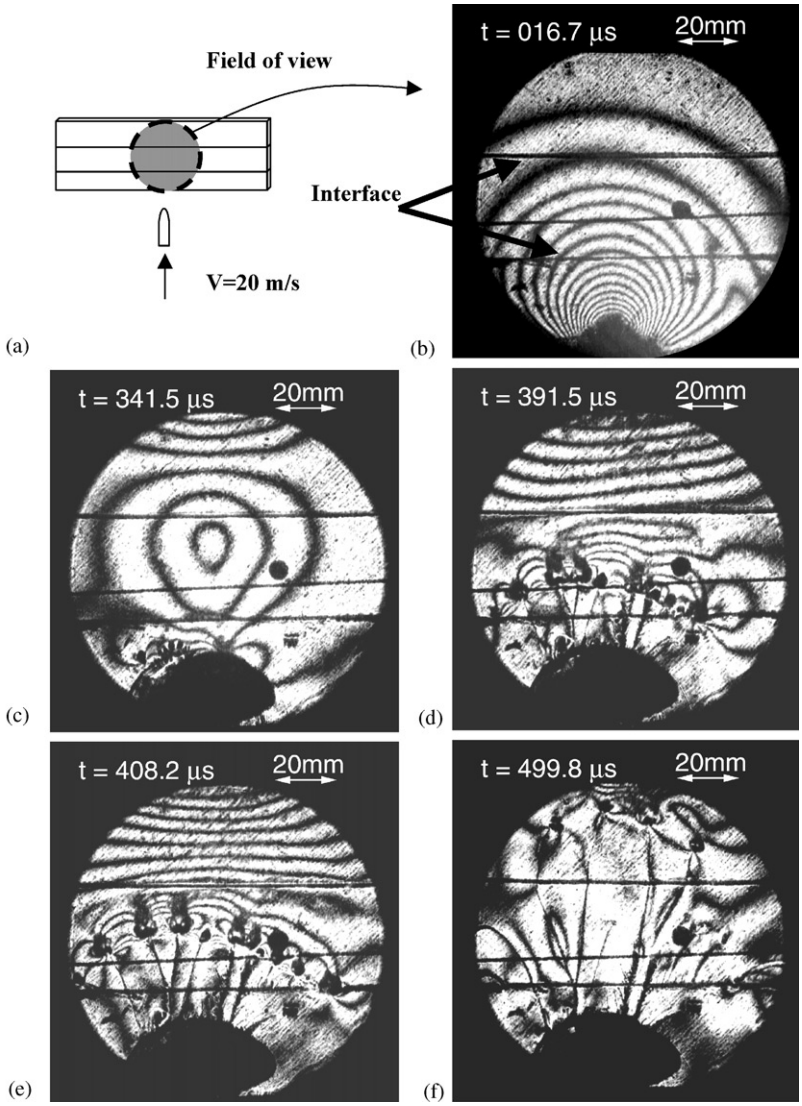

Fig. 16. Failure process of specimen 3LHHSP450384-3302. (The lower and upper thin lines are intermediate and strong interfaces.)

penetrate the intermediate strength bond of the lower interface (primarily near the center where the incident angle is large). Some interfacial debonding also occurs and is triggered by the radial cracks that approach the interface with more shallow angles. However, the situation at the upper, weak interface is very different. As radial cracks approach the weak bond, they are completely arrested neither penetrating nor causing debonding of this second interface. This is also found to be

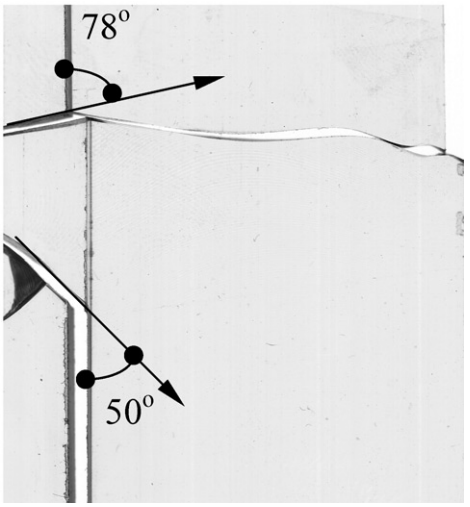

Fig. 17. Intra-layer cracks hit the interface with different angles (specimen 3LHHSP330384-3841). The crack with a large incident angle penetrated the interface while the crack with a small incident angle deflected at the interface.

true in all other cases (such as Fig. 18(b) and (c)) where such a weak and ductile bond is involved. In all of these cases, the bond was never penetrated nor was there any visible decohesion, at least at an impact speed of 21 m/s. This speaks of an apparent ductility of this bond whose extend will be investigated next.

In order to further test the impact resistance of specimens with 5083 weak but ductile adhesive bonds, a three-layer specimen containing two identical 5083 interfaces was designed and subjected to different impact speeds. The post-mortem pictures are shown in Fig. 19. The impact speeds were 20 and 46 m/s, respectively. Although the size of the local impact damage zone is quite different, in both cases the bond was again neither penetrated nor compromised. The impact damage is still limited inside the layer impacted directly by the projectile. The other two layers are still perfectly bonded.

To understand the effect of the introduction of a ductile adhesive bond as a mechanism for failure prevention, real-time visualization was undertaken in Fig. 20. As shown in Fig. 20(b), the stress wave intensity across the interface was reduced dramatically after the first interfacial 5083 bonding was encountered. In Fig. 20(c), the stress wave intensity was further reduced after the second 5083 interface was crossed. Meanwhile, complicated stress wave movement is seen in Fig. 20(d) and the dark contact zone is continuously growing. Radial cracks are initiated from the impact point very early (around 70 μs) compared to the other three-layer specimens shown in Fig. 16. However, those cracks soon arrested at the interface as seen in Fig. 20(e) and (f). No interfacial debonding was found in this type of specimens. In our investigation, only low-impact speed tests were conducted.

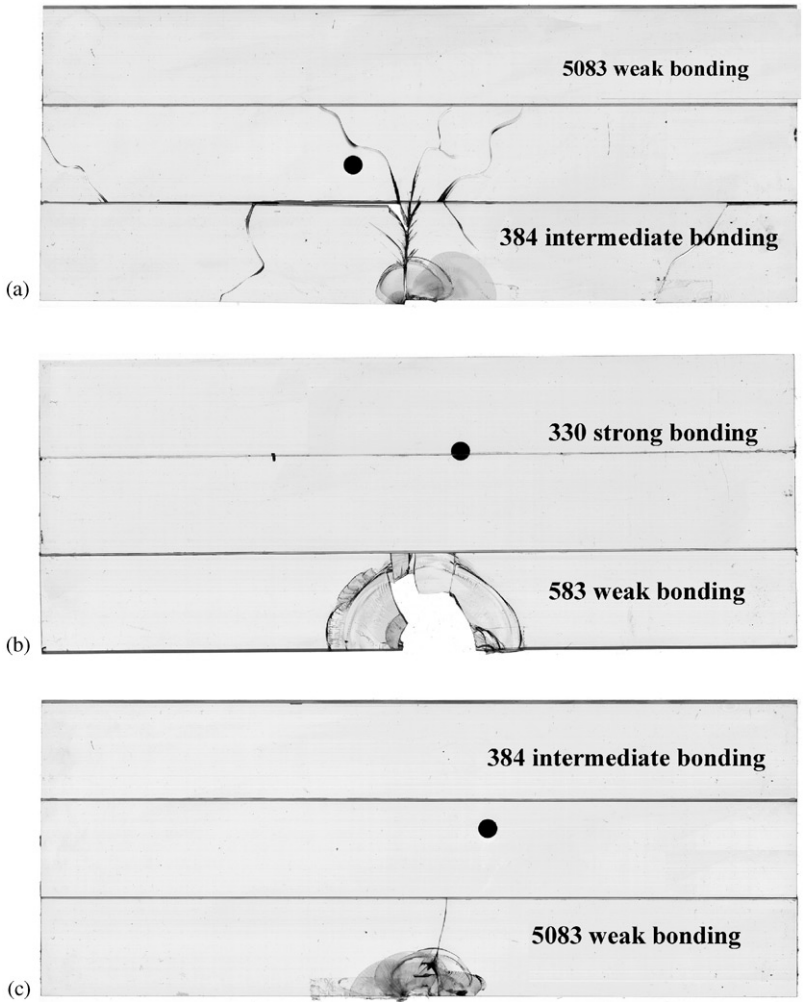

Fig. 18. Comparison of final pattern of the three-layer specimens with 5083 bonding with the same impact speed of 21 m/s. (a) 3LHHSP384583-3841, (b) 3LHHSP330583-5831, and (c) 3LHHSP384583-5831.

4. Summary and conclusions

We investigate the generation and time evolution of dynamic failure modes in layered materials composed of bonded layers of Homalite-100. We observe a variety of dynamic failure mechanisms in the form of either intra-layer (matrix) cracks or inter-layer (interfacial) cracks or debonding. Dynamic intra-layer failure is always of the symmetric (mode I) type and it often involves multiple branching events. Dynamic inter-layer fracturing or debonding is almost always shear-dominated and

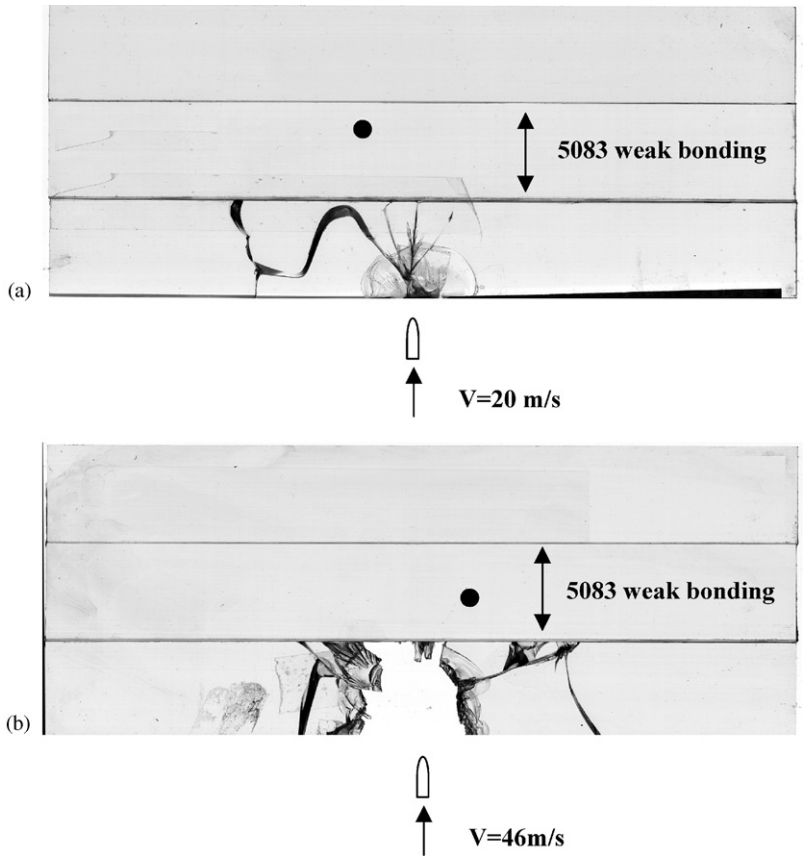

Fig. 19. Effect of the impact speed to failure patterns of the three-layer specimens featuring two weak but ductile adhesive bonds.

spreads at much faster speeds than intra-layer failure. One of the themes common to all cases studied here is the interrelation and interaction between these different symmetric and asymmetric failure modes. Indeed it is often the case that symmetric (mode I) intra-layer cracks approaching an interface (even if they never penetrate it) trigger mixed-mode or mode II interfacial delaminations, which in turn laterally spread mode I damage by an interesting mechanism of microcrack formation. In other cases, and depending on relative bond strengths and angles of incidence, intra-layer (matrix) cracks may clearly penetrate an interface without delaminating it.

In this paper, we explore some of these phenomena, and their interrelation, in perhaps the simplest, non-trivial, setting possible. We intentionally choose layers of identical material constitution in order to eliminate wave speed and other property mismatches across interfaces. We instead concentrate in varying bond strengths, layer geometry and to some extend impact speed. The above described, real-time

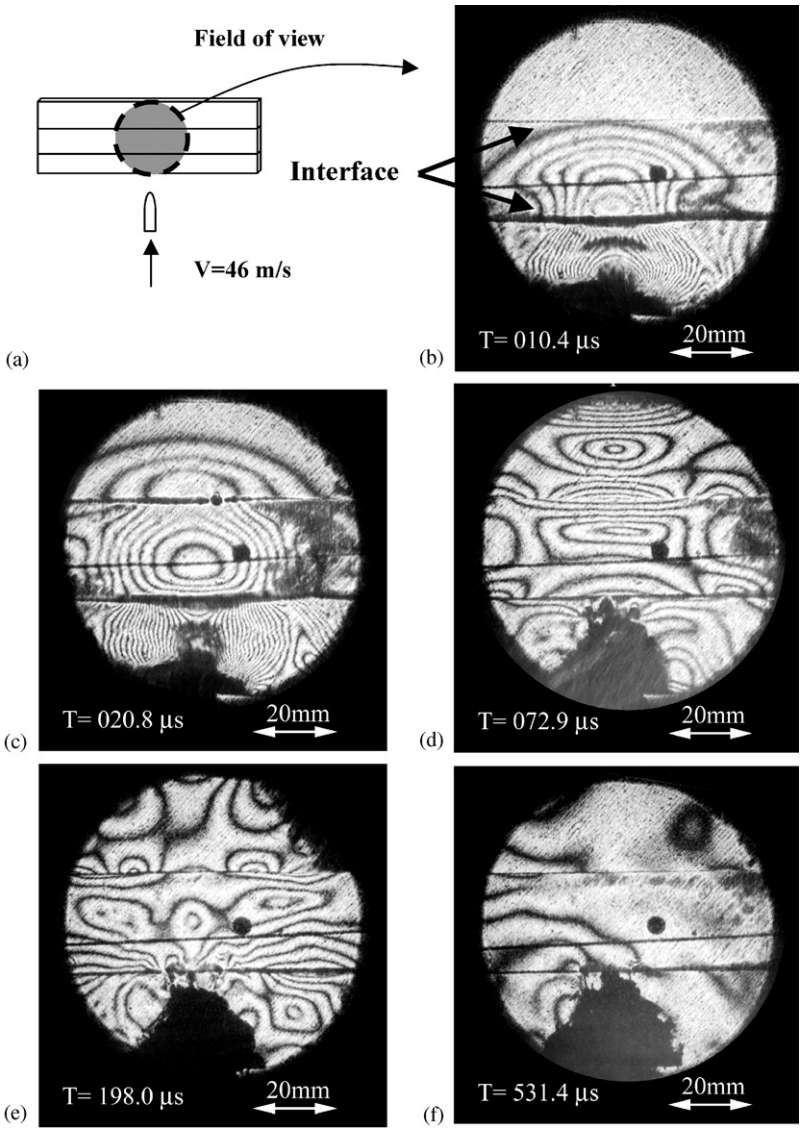

Fig. 20. Impact damage progress and wave propagation in a three-layer specimen featuring two 5083 weakly bonded interfaces (3LHHSP583-2).

observations of failure modes in layered solids, in addition to identifying some new basic failure phenomena, can perhaps serve as benchmark experiments for the validation of complex numerical codes designed to model dynamic failure of layered structures.

Acknowledgements

The authors gratefully acknowledge the support of the Office of Naval Research (Dr. Y.D.S. Rajapakse, Project Monitor) through a grant (#N00014-95-1-0453) to Caltech.

References

[1] Hutchinson JW, Suo Z. Mixed mode cracking in layered materials. Adv Appl Mech 1992;29:63–191.
[2] Abrate S. Impact on laminated composites: recent advances. Appl Mech Rev 1994;47:517–44.
[3] Takeda N, Sierakowski RL, Ross CA, Malvern LE. Delamination-crack propagation in ballistically impacted glass/epoxy composite laminates. Exp Mech 1982;22:19–65.
[4] Espinosa H, Lu H-C, Xu Y. A novel technique for penetrator velocity measurement and damage identification in ballistic penetration experiments. J Compos Mater 1998;32:722–43.
[5] Riley WF, Dally JW. A photoelastic analysis of stress wave propagation in a layered model. Geophysics 1966;31:881–99.
[6] Xu LR, Rosakis AJ. Impact failure characteristics in sandwich structures; Part I: Basic failure mode selection. Int J Solid Struc 2002;39:4215–35.
[7] Dally JW. Dynamic photoelastic studies of fracture. Exp Mech 1979;19:349–61.
[8] Kobayashi AS, Mall S. Dynamic fracture toughness of homalite-100. Exp Mech 1978;18:11–8.
[9] Ramulu M, Kobayashi AS. Mechanics of crack curving and branching—a dynamic fracture analysis. Int J Fract 1985;27:187–201.
[10] Ravi-Chandar K, Knauss WG. An experimental investigation into dynamic fracture. III. On steady-state crack propagation and crack branching. Int J Fract 1984;26:141–54.
[11] Xu LR, Samudrala O, Rosakis AJ. Measurements of Interfacial Mechanical Properties With the Aid of Two Optical Techniques, Proceedings of the 2002 SEM Annual Conference & Exposition on Experimental and Applied Mechanics, Society for Experimental Mechanics, Inc. Bethel, CT, USA, paper 34, 2002.
[12] Gordon JE. The new science of strong materials, 2nd ed.. London, UK: Pitman Publishing Limited, 1976.
[13] Rosakis AJ, Samudrala O, Coker D. Cracks faster than shear wave speed. Science 1999;284:1337–40.
[14] Needleman A. An analysis of intersonic crack growth under shear loading. J Appl Mech 1999;66: 847–57.
[15] Geubelle PH, Kubair D. Intersonic crack propagation in homogeneous media under shear-dominated loading: numerical analysis. J Mech Phys Solids 2001;49:571–87.
[16] Abraham FF, Gao H. How fast can cracks propagate? Phys Rev Lett 2000;84:3113–6.
[17] Rosakis AJ, Samudrala O, Coker D. Intersonic shear crack growth along weak planes. Mater Res Innovations 2000;3:236–43.
[18] Samudrala O, Huang Y, Rosakis AJ. Subsonic and intersonic shear rupture of weak planes with a velocity weakening cohesive zone. J Geophys Res, 2003. in press.
[19] Sun CT, Rechak S. Effect of adhesive layers on impact damage in composite laminates. In: Whitcomb, JD, editor. Composite materials: testing and design (eighth conference). ASTM STP 972. Philadelphia: American Society for Testing and Materials, 1988. p. 97–123.
[20] Xu LR, Huang YY, Rosakis AJ. Dynamic crack deflection and penetration at interfaces in homogeneous materials: experimental studies and model predictions, in preparation. J Mech Phys Solids 2003; in press.